

Bidirectional Photovoltage-Driven Oxide Transistors for Neuromorphic Visual Sensors

Chenxing Jin, Jingwen Wang, Shenglan Yang, Yang Ding, Jianhui Chang, Wanrong Liu, Yunchao Xu, Xiaofang Shi, Pengshan Xie, Johnny C. Ho, Changjin Wan, Zijian Zheng, Jia Sun,* Lei Liao,* and Junliang Yang*

Biological vision is one of the most important parts of the human perception system. However, emulating biological visuals is challenging because it requires complementary photoexcitation and photoinhibition. Here, the study presents a bidirectional photovoltage-driven neuromorphic visual sensor (BPNVS) that is constructed by monolithically integrating two perovskite solar cells (PSCs) with dual-gate ion-gel-gated oxide transistors. PSCs act as photoreceptors, converting external visual stimuli into electrical signals, whereas oxide transistors generate neuromorphic signal outputs that can be adjusted to produce positive and negative photoresponses. This device mimics the human vision system's ability to recognize colored and color-mixed patterns. The device achieves a static color recognition accuracy of 96% by utilizing the reservoir computing system for feature extraction. The BPNVS mem-reservoir chip is also proposed for handing object movement and dynamic color recognition. This work is a significant step forward in neuromorphic sensing and complex pattern recognition.

human visual system is better at processing image data for classification and recognition.^[6–8] The human retina collects and processes a large amount of external information before forming a visual image in the brain.^[9–12] Inspired by the human eye, neuromorphic vision sensors are being studied to meet the ever-increasing requirements for image processing.^[4,13–15] The development of artificial vision systems requires devices that can independently adapt to external optical stimuli and perform information processing. However, emulating biological vision requires complementary photoexcitation and photoinhibition, which is challenging to achieve with a single device.^[16,17] Therefore, designing neuromorphic visual sensors with both positive and negative photoresponse (PPR and NPR) effects is highly pursued.^[18–21] Walia et al. exploited the unique photoresponse

1. Introduction

The rapid advancement of artificial intelligence has increased the demand of modern intelligent systems for artificial vision systems.^[1–5] In comparison to conventional artificial vision, the

produced by oxidation-related defects in 2D black phosphorus phototransistors to achieve light-wavelength-reconfigurable excitatory/inhibitory behaviors.^[22] Miao et al. developed a neuromorphic visual sensor that uses the gate-tunable PPR and NPR of 2D van der Waals (vdW) vertical heterostructures.^[23] Zhai et al.

C. Jin, J. Wang, S. Yang, Y. Ding, J. Chang, W. Liu, Y. Xu, X. Shi, J. Sun, J. Yang
Hunan Key Laboratory for Super Microstructure and Ultrafast Process
School of Physics
Central South University
Changsha, Hunan 410083, P. R. China
E-mail: jiasun@csu.edu.cn; junliang.yang@csu.edu.cn

C. Jin, J. Wang, W. Liu, Y. Xu, X. Shi, J. Sun
State Key Laboratory of Precision Manufacturing for Extreme Service
Performance
College of Mechanical and Electrical Engineering
Central South University
Changsha, Hunan 410083, P. R. China

C. Jin, J. Wang, W. Liu, Y. Xu, X. Shi, J. Sun
State Key Laboratory of Transducer Technology
Shanghai Institute of Microsystem and Information Technology
865 Changning Road, Shanghai 200050, P. R. China

P. Xie, J. C. Ho
Department of Materials Science and Engineering
City University of Hong Kong
Kowloon, Hong Kong SAR 999077, P. R. China

C. Wan
School of Electronic Science & Engineering
and Collaborative Innovation Centre of Advanced Microstructures
Nanjing University
Nanjing, Jiangsu 210093, P. R. China

Z. Zheng
Department of Applied Biology and Chemical Technology
Faculty of Science
The Hong Kong Polytechnic University
Hong Kong SRA 999077, P. R. China

L. Liao
State Key Laboratory for Chemo/Biosensing and Chemometrics
College of Semiconductors (College of Integrated Circuits)
Hunan University
Changsha 410082, P. R. China
E-mail: liao lei@whu.edu.cn

The ORCID identification number(s) for the author(s) of this article can be found under <https://doi.org/10.1002/adma.202410398>

DOI: 10.1002/adma.202410398

proposed an in-sensor broadband convolutional processing system based on a 2D vdW PdSe₂/MoTe₂ heterojunction. The proposed device demonstrated photodetection over a wide spectral range, as well as electric-field-tunable PPR and NPR effects.^[24] Although these findings demonstrate the feasibility of bidirectional synaptic modulation via all-photonic stimulation, more research is needed to develop high-efficiency and high-density scalable system architectures that are not subject to material scalability.^[18,25] This problem can be solved by using a photovoltaic transistor (PVT) with two modules: a photovoltaic and a neuromorphic transistor. The key to this structure is to integrate sensing and biomimetics, with the PV module providing photovoltage in response to light excitation and the transistor generating a neuromorphic electrical signal.^[12,26–28] The electrolyte material in ion-regulated oxide transistors can form a nanoscale electric double layer, allowing for operation in a low voltage range of 0.5–2 V.^[29–31] In addition, many researchers have used ion-regulated oxide transistors to simulate biological functions because the ion movement phenomenon is very similar to biological behavior.^[32] When the oxide channel layer is exposed to light, the PPR is most visible in the ion-regulated oxide transistor; however, the PPR and NPR effects have not been observed simultaneously in a single device. Perovskite photoelectronic devices have recently attracted increased research attention due to their excellent optoelectronic properties, such as a high absorption coefficient, tunable bandgap, high carrier mobility, long carrier lifetime, and diffusion length.^[33–37] The perovskite solar cells (PSCs) can achieve a power conversion efficiency (PCE) of 25%.^[38–40] Interestingly, the PSCs can produce a stable voltage of ≈ 1 V, which is sufficient to drive ion-regulated oxide transistors.^[41] The integrated unit of PSCs and ion-regulated oxide transistors exhibits great promise for simulating biological vision in the visible spectrum.^[26,27]

We present a bidirectional photovoltage-driven neuromorphic visual sensor (BPNVS) constructed by monolithically connecting the different electrodes of two PSCs to the two gates of ion-regulated In₂O₃ transistors. Under photostimulation, the proposed device can induce both PPR and NPR. The BPNVS, which uses a tunable photoresponse, can simulate excitatory and inhibitory behavior similar to biological vision. Because of the large storage capacity of the ion-regulated transistors, the proposed BPNVS exhibits a non-volatile multi-level optoelectronic memory effect. In addition, a reservoir computing (RC) system based on BPNVS is developed to classify various colors and handwritten digits. The neural network has a static color recognition accuracy of nearly 96%. Furthermore, we propose to develop a mem-reservoir (MR) chip and a data processing model based on the BPNVS to achieve motion-color detection similar to the human retina. These results demonstrate that BPNVS has a high potential for practical applications in future visual systems.

2. Results

2.1. Design of BPNVS

The visual system is one of the most important sensory systems in humans, making up one-third of the cerebral cortex. The retina, lateral geniculate body, and visual cortex are the most

important components of the visual system (Figure 1a). Light takes information from the external world and projects it onto the retina at the bottom of the eye. The photoreceptor cells of the retina convert light signals into electrical signals (Figure 1a–i). The photoreceptor cells in the retina include rod cells and cone cells. Cone cells can encode “color” information because their various types are sensitive to different colors of light (blue, red, and green) (Figure 1a–ii).^[42–44] The receptive field is an important concept in the visual system, and each cell has its own receptive field, which is the area where cells can be stimulated or inhibited. For example, feedback from horizontal cells provides the optic nerve cells with a central peripheral antagonistic receptive field (Figure 1a–iii). When light stimulates the central area of a cell’s receptive field, it becomes excited, whereas the surrounding cells become inhibited and inactive. In contrast, Off-cell shows the exact opposite behavior. After preliminary processing, the retina transmits signals to the brain by ganglion cells.^[45,46] The lateral geniculate body is where the visual information enters the brain before being processed and integrated to produce key visual information. This key visual information is then transmitted to the primary visual cortex for further extracting important features (Figure 1a–iv), such as spatial orientation information (speed, color, direction, etc.) of visual shapes (Figure 1a–v). A BPNVS is proposed to perform functions such as color recognition and movement detection. The structure of the BPNVS device is shown in Figure 1b. The BPNVS unit consists of three main devices: two PSCs and a dual-gate ion-regulated In₂O₃ transistor. PSCs function as photoreceptors, converting external photo stimuli into electrical signals. The ion-regulated In₂O₃ transistor is classified as a neuromorphic signal processing unit. The electrical signals from the two PSCs are then routed to two transistor gates, causing electron accumulation/exhaustion in the In₂O₃ channel and, as a result, current ascent/descent. When used as a visual sensor, PSCs receive a control optical signal and read out the current signal of transistor device using a channel voltage (V_{ds}).

2.2. Photoelectric Performance and Simulation of Synaptic Function

The dynamic output signal of the device is generated by the drain-source currents (I_{ds}). However, when different PSC electrode terminals are connected to the gate of the oxide transistor, the transfer curves of the In₂O₃ transistor show different photoelectric response behaviors (Figure 2a,b). When the ITO electrode is connected to the gate of an In₂O₃ transistor, the transfer curve gradually shifts to the right as the optical power density increases (Figure 2a). The gate voltage (V_{gs}) scanning range of the transfer curve is -5 – 2 V, and V_{ds} is set to 0.1 V. Conversely, the transfer curve shifts to the left when the Ag electrode is connected to the In₂O₃ transistor (Figure 2b). The light/dark current ratio (I_{light}/I_{dark}) is calculated and shown in Figure 2c (where $V_{gs} = -1.7$ V in Figure 2a and $V_{gs} = -3$ V in Figure 2b). The BPNVS clearly exhibits typical PPR and NPR behavior as the optical power density increases. In addition, 405 nm and 648 nm wavelengths are used to repeat the above-mentioned test in the visible spectrum, and PPR/NPR is still detected (Figures S1 and S2, Supporting Information). However, because PSCs respond

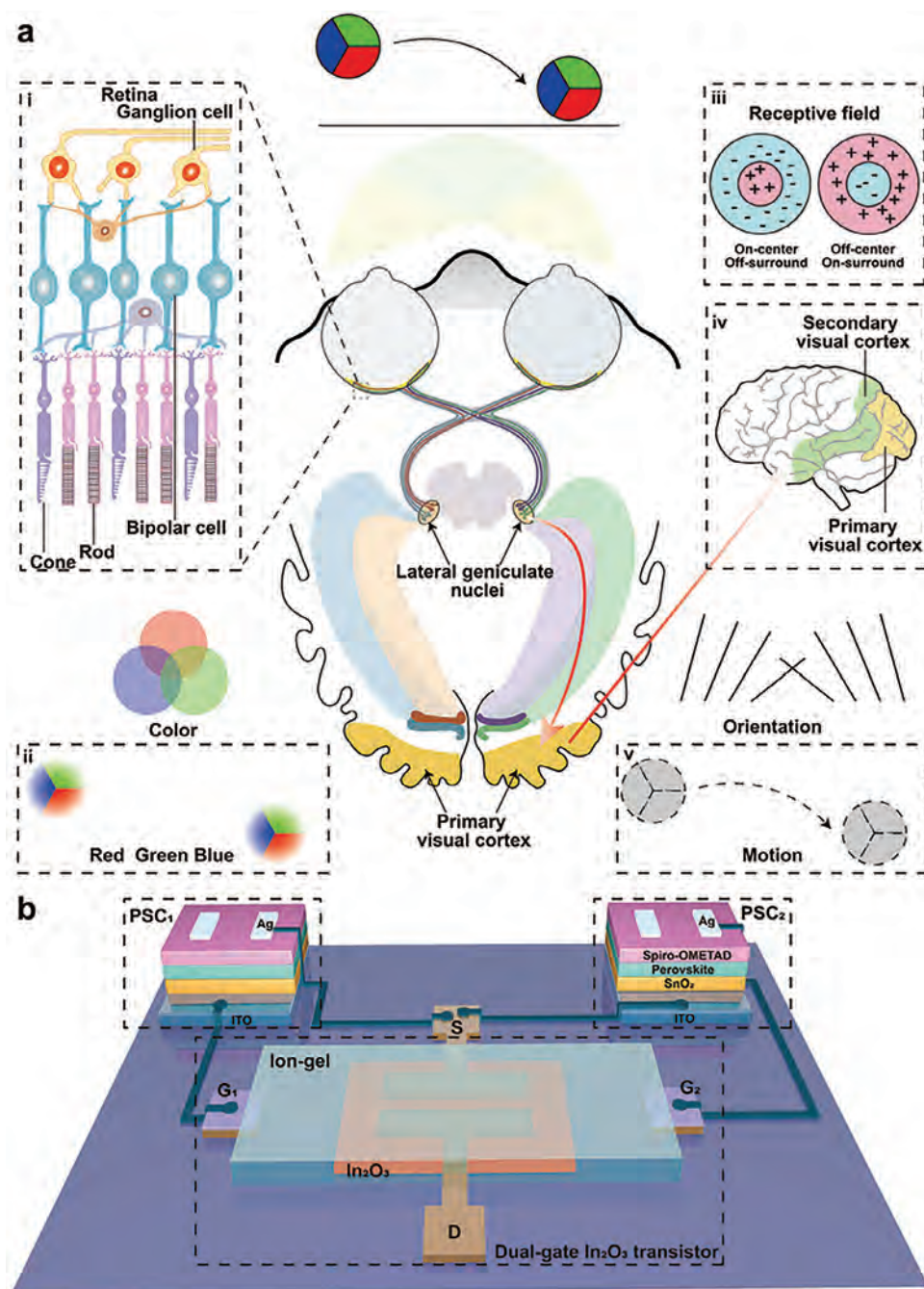


Figure 1. BPNVS. a) Schematic diagram of the human visual system. Insert: i) Structural diagram of the retina. ii) Schematic diagram of the color recognition system. iii) Example image of the receptive field. iv) A schematic diagram of the secondary/primary visual cortex in the human brain. v) Schematic diagram of object motion recognition. b) Structure scheme of BPNVS and working principle.

differently to different wavelengths of light, $I_{\text{light}}/I_{\text{dark}}$ varies accordingly. Clearly, PPR and NPR can be implemented in BPNVS with proper regulation. Unless otherwise specified, all illumination wavelengths used in work are 520 nm. Note a large hysteresis window and high current switching ratio, which could be caused by trapping and release of charges.^[47,48] As a perception unit of BPNVS to the outside world, the ability of PSCs to receive light stimuli and output a stable voltage signal is crit-

ical for regulating In₂O₃ transistors. Therefore, the photoelectric properties of PSCs are assessed. The SEM images show that the perovskite absorber layer is extremely flat (Figure S3a, Supporting Information). The cross-sectional of the PSC device shows the thickness of each layer (Figure S3b, Supporting Information). The absorption spectrum of the perovskite layer demonstrates that the PSCs have a broad photoresponse range (Figure S3c, Supporting Information). During testing, the

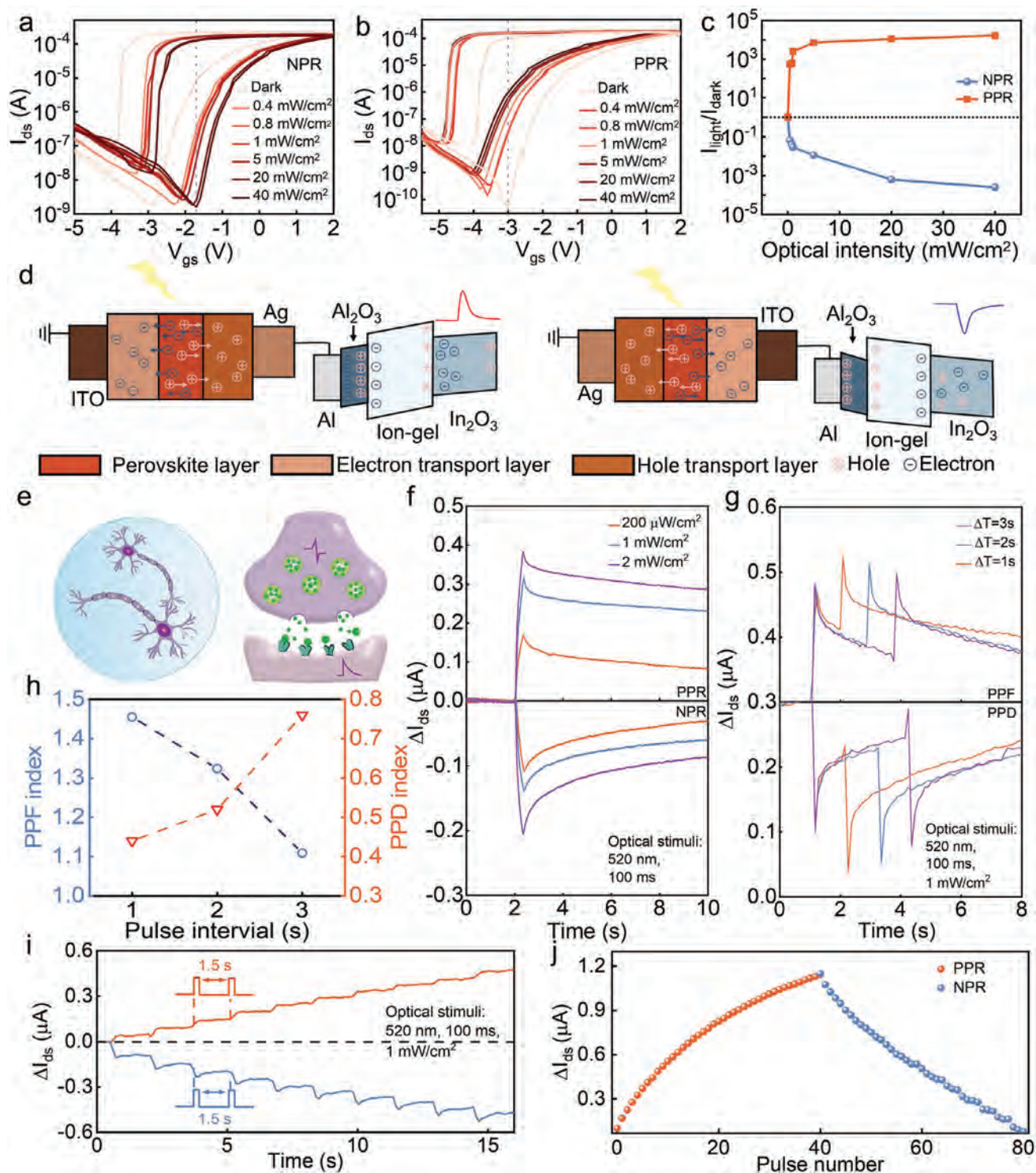


Figure 2. Photoelectric performance and simulation of the synaptic function. a) Variation of the transfer curve when the ITO electrode is connected to the gate of the In_2O_3 transistor under light ($\lambda = 520 \text{ nm}$). b) Variation of the transfer curve when the Ag electrode is connected to the gate of the In_2O_3 transistor under light ($\lambda = 520 \text{ nm}$). c) $I_{\text{light}}/I_{\text{dark}}$ current ratio versus optical intensity, where the $I_{\text{light}}/I_{\text{dark}}$ current ratio is extracted from $V_{\text{gs}} = -1.7 \text{ V}$ in Figure a and $V_{\text{gs}} = -3 \text{ V}$ in Figure b. d) Band structure diagrams of PPR and NPR. e) Simplified structures of biological neurons and synapses. f) ΔI_{ds} of excitation/inhibition caused by light pulses with different intensities at $V_{\text{ds}} = 0.01 \text{ V}$ (for optical intensity of $200 \mu\text{W cm}^{-2}$, 1 mW cm^{-2} , and 2 mW cm^{-2} , and light pulse width of 100 ms). g) PPF and PPD measurement shows the ΔI_{ds} change caused by two consecutive light pulses (1 mW cm^{-2} , $V_{\text{ds}} = 0.01 \text{ V}$, and light pulse width = 100 ms) with different time interval ($1, 2$, and 3 s). h) PPF index and PPD index as a function of time interval. i) Progressive multi-level memory states configured with PPR and NPR (light pulse width = 100 ms , light pulse intervals = 1.5 s , and $V_{\text{ds}} = 0.01 \text{ V}$). j) Linear variation of the PPR and NPR with the number of pulses.

current density of PSCs stabilized at $23.67 \text{ mA}\cdot\text{cm}^{-2}$, resulting in a higher PCE of 20.42% (Figure S3d, Supporting Information). PSC is considered a two-terminal optoelectronic device, and its output voltage is tested at various optical power densities (Figure S3e,f, Supporting Information). First, using the Ag electrode as input, the PSC outputs a stable positive voltage within 0–1 V at various optical power densities (Figure S4a, Supporting Information). The temporal voltage response of PSC is also investigated (Figure S4b, Supporting Information). The PSC's voltage response has good repeatability and a response time of 28 ms (Figure S4c, Supporting Information). Similarly, a stable negative output voltage of -1–0 V and a fast voltage response time of 28 ms could be obtained with an ITO electrode as the input (Figure S4d–f, Supporting Information). These results demonstrate that PSCs have a stable voltage input and a fast voltage response, which is useful for further research into BPNVS. We prepared the integrated BPNVS array using the flowchart shown in Figure S5 (Supporting Information). The BPNVS array contains 18 PSCs and 9 In_2O_3 transistors. An independent BPNVS is made up of an In_2O_3 transistor and two PSCs (Figure S6, Supporting Information). Every In_2O_3 transistor in the BPNVS array is tested. All transfer curve images have a large hysteresis window and a high current switching ratio ($\sim 10^4$) (Figure S7, Supporting Information). In addition, temperature-dependent characteristics are tested as key evaluation parameters for transistors (Figure S8, Supporting Information).^[49,50] These results further highlight the enormous potential of BPNVS in large-scale integrated preparation. To delve deeper into the simulation of basic neuroplasticity functions by BPNVS, the PPR and NPR mechanisms are discussed. The Al electrode of the In_2O_3 transistor is naturally oxidized, resulting in an Al_2O_3 layer with high-density deep defect states capable of capturing and releasing positive charges.^[47,48] The defect states in Al_2O_3 can be removed or filled by adjusting the Fermi level of the gate metal. When the Ag electrode is connected to the In_2O_3 transistor, only the photogenerated positive charge of the PSC can pass through the spiro-OMETAD hole transport layer under light before being conducted to the transistor's gate. As a result, a positive pulse acts on the gate of the In_2O_3 transistor, which accumulates electrons significantly at the interface of the ion-gel/ In_2O_3 semiconductor, causing the I_{ds} to increase (Figure 2d left). At the same time, the positive charge remains trapped in the Al_2O_3 layer, allowing I_{ds} to be stored for an extended time after the pulse. On the contrary, when the ITO electrode is connected to an In_2O_3 transistor, only photogenerated electrons from the PSC can pass through the SnO_2 electron transport layer and be conducted to the gate of the transistor under illumination. As a result, a negative pulse acts on the gate of the In_2O_3 transistor, causing the trapped positive charges in Al_2O_3 to be removed. The electrons at the ion-gel/ In_2O_3 semiconductor interface are reduced, as is I_{ds} (Figure 2d right). Synapses are a special structure in the nervous system that allows neurons to transmit chemical or electrical signals to another neuron (Figure 2e). As a result, the basic neuroplasticity function of BPNVS is achieved. The effect of light intensity on photoexcitation/inhibition behavior is quantitatively assessed (Figure 2f). Increasing the intensity of a light pulse increases photoexcitation/photoinhibition (ΔI_{ds}). When the Ag electrode is connected to the gate, the device's ΔI_{ds} increase from 0.17 to 0.38 μA , indicating a PPR. When the ITO elec-

trode is connected to the gate, the device ΔI_{ds} show a reverse increase from -0.11 to -0.20 μA , exhibiting an NPR. The ΔI_{ds} are tested with different light intensities using 405 and 648 nm wavelength light sources (Figure S9, Supporting Information). In addition, the variation of ΔI_{ds} with optical pulse duration is obtained at the same optical power density (Figure S10, Supporting Information). Paired-pulse facilitation (PPF) and paired-pulse depression (PPD) are important neuroplasticity characteristics that are required for visual information recognition and decoding in an artificial neural system.^[51,52] PPF/PPD refers to the increase/decrease of I_{ds} , where the peak of the I_{ds} activated by the second light pulse (A_2) is greater/less than that of the first light pulse (A_1).^[53] Here, the PPF/PPD index is defined as A_2/A_1 , which is closely related to the time interval between two successive light pulses. Figure 2g shows that the BPNVS exhibits typical PPF and PPD behavior when simulated with two consecutive light pulses (light pulse width = 100 ms, optical power density = 1 mW cm^{-2}). The PPF/PPD index increases/decreases with increasing pulse time intervals (Figure 2h). Under multiple light pulses, the BPNVS can cause stronger non-volatile increase or decrease of neuromorphic behavior. The multi-level memory states are also tested and shown in Figure 2i. When ten consecutive pulses (light pulse interval = 1.5 s, light pulse width = 100 ms) are applied to the device, both light increase and decrease exhibit progressive multi-level memory states. In addition, we demonstrated progressive multi-level memory states under 20 consecutive pulses (Figure S11, Supporting Information). Furthermore, the multi-level memory state changes caused by 40 consecutive light enhancements followed by 40 consecutive light suppressions are also investigated (Figure S12, Supporting Information). The peak current after optical pulses is calculated as a function of pulse number, revealing a nearly linear correlation (Figure 2j). Obviously, the enhancement/suppression of current is achieved by applying light stimulation to the PSC, which will help in the development of the artificial neural network.

2.3. Visual Recognition Function Based on BPNVS

The RC system uses dynamic reservoirs with short-term memory to map temporal input features into a high-dimensional feature space.^[54,55] The readout function layer can efficiently analyze the mapped features for tasks like classification and time series analysis.^[56,57] Because only the readout layer needs to be trained, the system can efficiently process complex time series data while incurring minimal training costs. Figure S13 (Supporting Information) depicts the architecture of the RC system, which consists of the data preprocessing, RC, feature extraction, and training linear model modules. We used a BPNVS array to create an experimental reservoir. Figure 3a shows a schematic diagram of the RC system based on this architecture. First, the input signal is pre-processed and then converted into a series of photo-pulses through an algorithm. Each frame of the input signal generates a pulse train with a total length of τ and a pulse width of δ , which occurs in the data preprocessing module (Figure S13, Supporting Information). Consider [101101] as an example. At time $t = k$ during the input process, the node receives the value 1 from the pulse string. At time $t = k+1$, the value 0 in the pulse string

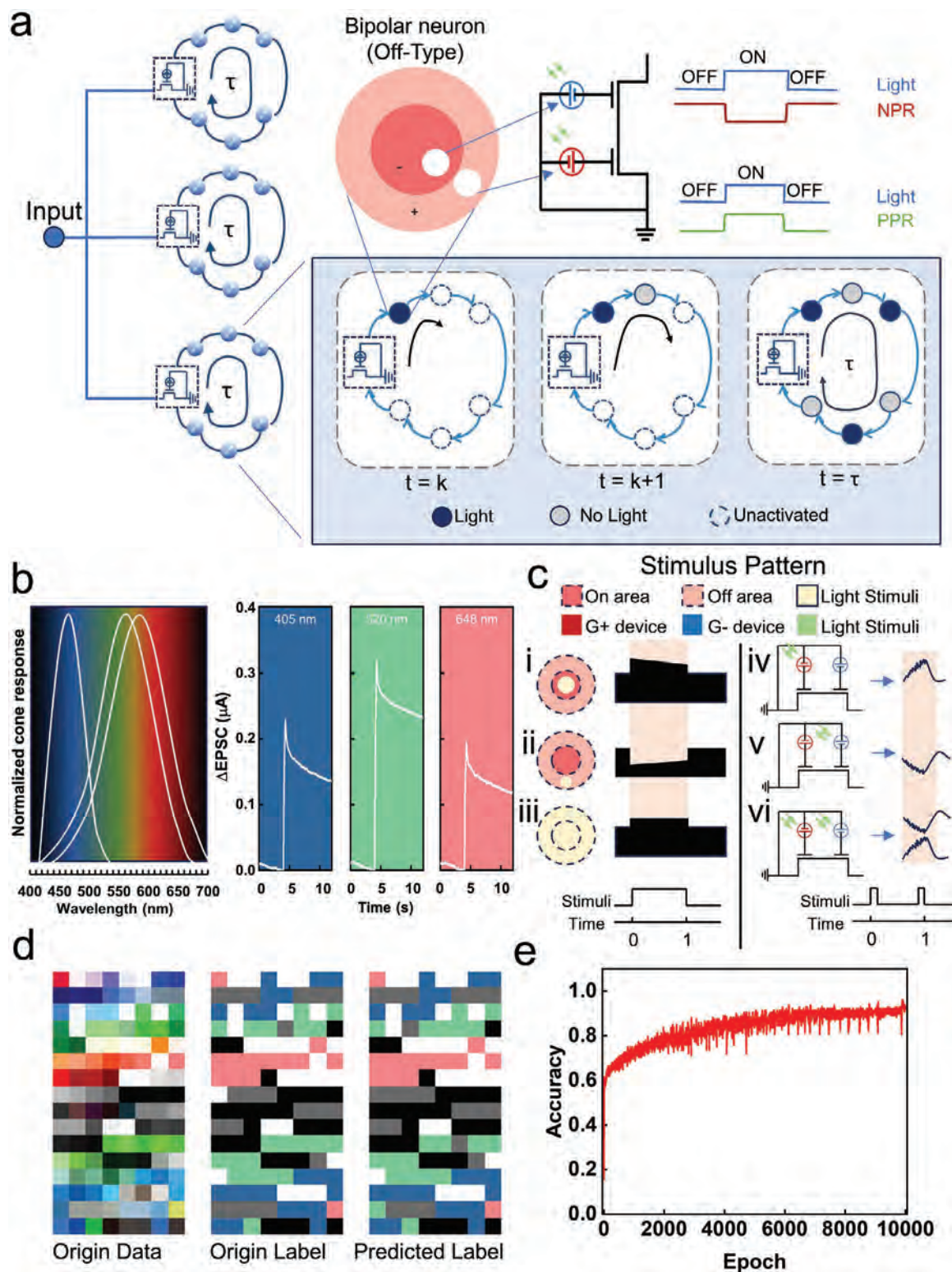


Figure 3. RC system based on BPNVS. a) Schematic diagram of a dynamic RC system based on a BPNVS. For a given input, the input image is divided into three channels that are fed to BPNVS. The response of the BPNVS over a duration τ is selected as a neuron node. b) Comparison of the photo-response of the optic cones in the retina of the human eye to different wavelengths of light with the current response of BPNVS to different wavelengths of light. c) Responses of retinal rod cells in the central-peripheral receptive field to different light situations in comparison to the current response of BPNVS in different light conditions. d) Origin data of color datasets, origin color labels, and predicted color labels. e) The evolution of classification accuracy during the training procedure.

means that no light is applied to the node, and the device retains the previous response state. The procedure continues until time $t = \tau$. This process occurs in the RC module (Figure S13, Supporting Information). When exposed to light, the NPR-enabled devices in these nodes respond negatively. This corresponds to the receptive field center of an Off-type bipolar cell becoming inactive when exposed to light. In contrast, devices with PPR generate a positive response when exposed to light. This corresponds to the off-type bipolar cell's receptive field becoming active when exposed to light. Figures S14 and S15 (Supporting Information) show the final results as well as the intermediate state of the reservoir to demonstrate the applicability of the RC system in image recognition and hand gesture recognition. This is achieved by performing various preprocessing operations on the input images before classifying and recognizing them using the reservoir for various tasks. The MNIST dataset achieves a recognition accuracy of 90.85%, while the DVS128 gesture dataset achieves 100%. This demonstrates that the photoreceptor reservoir can not only recognize images but also perform time-series gesture recognition tasks. The human eye's cone cells can perceive different colors of light, which are classified as short, medium, and long waves. The short wave represents blue light, the medium-wave represents green light, and the long wave represents red light (Figure 3b). BPNVS has distinct photoresponses to red, green, and blue (RGB) illumination at excitation wavelengths of 648 nm (R), 525 nm (G), and 405 nm (B), respectively. As a result, BPNVS can mimic the function of red, green, and blue sensing cone cells of the human retina. BPNVS can also mimic optic rod cells, which detect light intensity (Figure 3c). Cells in the receptive fields of optic nerve cells have center-periphery antagonistic properties and can be classified into two types: On-type and Off-type (e.g., Off-type in Figure 3a). Photo stimulation can excite the central region of the receptive field of On-type cells while inhibiting and transforming the surrounding cells into an inactive state. In Figure 3c–i, the receptive field center is photo-stimulated in the same way that a photo-stimulus is applied to a PPR device (Figure 3c–iv), resulting in a positive response. In Figure 3c–ii, the periphery of the receptive field is photo-stimulated, similar to a photo-stimulus applied to an NPR device, resulting in a negative response (Figure 3c–v). In Figure 3c–iii, both the center and the periphery of the receptive field are photo-stimulated simultaneously, similar to a photo-stimulus applied to both the PPR and NPR devices (Figure 3c–vi), resulting in a slightly lower positive response than the results shown in Figure 3c–i,iv. Next, the effectiveness of the reservoir for color recognition is verified. First, a small color dataset was created. The original color dataset was labeled and visualized to generate the origin label map (displayed on the left and middle in Figure 3d). The RC system then predicts labels for various colors, as shown on the right in Figure 3d. Using the label “Red” as an example, if the RGB value of one pixel is [255,0,0] and the corresponding label value is 0 (0 representing “Red”), the label 0 is replaced by [255,0,0] during the visualization process. This enables an intuitive representation of the data labels and prediction labels. The RC system based on BPNVS devices achieved color recognition accuracy of up to 96% (Figure 3e). The color recognition accuracy is tested using a real image of the cube in various color combinations (Figure S16, Supporting Information). The RC system can accurately recognize colors.

2.4. Motion and Color Detection Based on BPNVS MR Chip

Furthermore, the RC system of BPNVS successfully recognizes images, gestures, and colors. A concept of an MR chip is proposed (Figure S17, Supporting Information). Real-time color recognition of moving objects can be achieved using a series of internal circuits in an ideal MR chip that processes photo input. To perform the computation of motion-color recognition, the BPNVS array is configured as a matrix to generate the MR based on simulation, as shown in Figure 4a. Figure 4b shows a schematic diagram of the sub-reservoir circuit used in motion detection, which corresponds to the two sub-pixels on the blue box line in Figure 4a. Figure S18 (Supporting Information) shows the effect of motion recognition at various voltage threshold values (V_{th}). Adjusting V_{th} allows for the optimization of the motion detection effect in various scenarios. Figure 4c depicts the sub-reservoir circuit, which corresponds to the three sub-pixels in the red box shown in Figure 4a. The detailed procedure is described in the Methods section. The multitasking RC system uses a motion recognition procedure to detect moving objects (Figure 4b). When a moving object is detected, the pixels corresponding to the object are converted into photo-pulses and fed into the sub-reservoir for color classification. Subsequently, the color of the moving object is recognized (Figure 4c). Figure 4d shows that the output is zero when every two frames are static. When motion behavior is detected, the output displays the motion track. Figure 4e depicts the color recognition results of the moving object. The shape of the right hand, as well as the color of the gloves, is easily discernible. The BPNVS can serve as a retina-like hardware system, capable of sensing both static and moving objects, as well as extracting and processing color information, making it a viable candidate for a compact and efficient retinal vision sensor.

3. Conclusion

In this paper, we present a configurable BPNVS based on the monolithic integration of PSCs and dual-gate ion-regulated oxide transistors. When PSCs are exposed to light, tunable photoresponse behavior is observed. Because of the excellent storage performance of BPNVS, excitatory/inhibitory biological behaviors and a multi-level photoelectronic memory function are achieved. An RC system is also constructed using the proposed BPNVS, which can be used to extract the image's feature values. Various features of handwritten digits and gestures are recognized, with a static color recognition accuracy of 96%. Subsequently, we proposed a model for motion-color detection using the prepared BPNVS MR chip. To determine whether an object is moving, the output voltage of the motion detection sub-reservoir is compared to the threshold V_{th} . After detecting movement, the color of the moving object will be identified. The proposed BPNVS increases the possibilities for expanding the application of human eye bionic design while also encouraging further development of neuromorphic visual systems.

4. Experimental Section

Fabrication of Dual-Gate Ion-Regulated Oxide Transistors: The glass substrate is thoroughly cleaned by sonication in water containing detergent, deionized water, acetone, and isopropanol for 30 minutes per step.

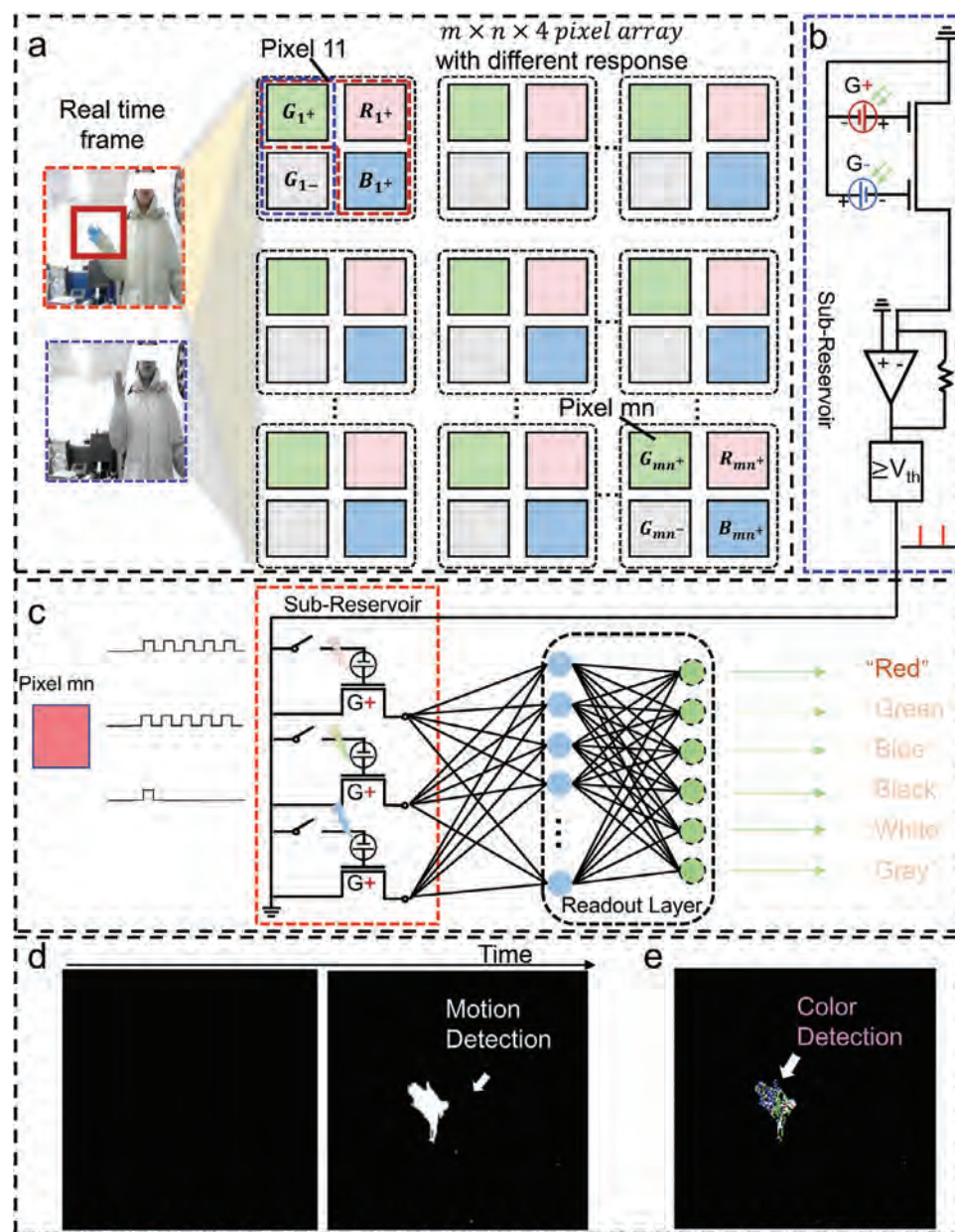


Figure 4. Motion and color detection based on BPNVS MR chip. a) MR chip pixel array for color and motion recognition. b) Illustration of sub-reservoir circuit diagram used for motion detection. c) The corresponding sub-reservoir circuit for color recognition of a single pixel. d) The output signal at the end of the pixel sensing process. e) Color recognition of moving subjects.

The substrate was dried in an oven at 85 °C for two hours. A thin film of a semiconductor In_2O_3 was deposited on the glass substrate. The pressure in the magnetron sputtering chamber was kept below 8×10^{-4} Pa. Next, argon and oxygen were mixed in a specific gas volume flow ratio (40:4 sccm) and introduced into the sputtering chamber. The working pressure of the sputtering chamber was then set to 1 Pa, the working power to 50 W, the sample rotation speed to 20 rpm/min, and the sputtering time to 3 minutes. The source-drain and gate electrodes were then patterned with a mask on a glass substrate before 50 nm-thick Al electrodes were deposited using thermal evaporation. To create an ionic gel, the polymer, ionic liquid, and acetone were mixed in a weight ratio of 1:4:6, stirred, and heated at 60 °C for 8 hours. Finally, using a printing technique, the ionic gel was applied to a semiconductor chan-

nel layer and a portion of the gate electrode to create an oxide synaptic device.

Fabrication of PSCs: The devices are fabricated with the structure ITO/ SnO_2 /Perovskite/Spiro-OMETAD/Ag using SnO_2 nanoparticles as an electron transport layer (ETL). To fabricate the perovskite layer, a two-step spin coating method that involves the interdiffusion of lead halide and organic salts was used. SnO_2 colloid solution (2.67%) is spin-coated on a prepared ITO substrate at 3000 rpm for 30 seconds and then annealed in ambient air at 150 °C for 30 minutes. Following that, 1.3 M of PbI_2 in DMF:DMSO (volume ratio 9.5:0.5) was spin-coated onto SnO_2 at 1500 rpm for 30 s, followed by annealing at 70 °C for 30 minutes in a nitrogen atmosphere. After cooling to room temperature, the FAI: MACI: MABr mixture solution (60 mg: 6 mg: 6 mg in 1 mL IPA) was spin-coated onto the PbI_2 at

1500 rpm for 30 seconds, thermally annealed at 150 °C for 20 minutes in ambient air (under 40% humidity). The hole transporting layer (HTL) was deposited on top of the perovskite layer with a spin speed of 3000 rpm for 30 seconds using a spiro-OMETAD solution. Finally, a 100 nm silver film was thermally evaporated as a counter electrode using a shadow mask with an active area of 0.105 cm².

Characterization and Electrical Performance Measurement of the Device: The electrical performance and neuromorphic functions of the BPNVS were then characterized using a semiconductor parameter analyzer (Keithley 4200-SCS) in the air at room temperature. Laser diodes with different wavelengths (405, 520, and 648 nm) were used to irradiate the PSC and generate output voltage. The morphologies of the as-prepared perovskite material were investigated using an atomic force microscope (5500 AFM, Agilent technology). A UV-vis spectrophotometer (UV-vis, Puxi, T9, China) was used to obtain the absorption spectra of perovskite absorber layers. The current density and power conversion efficiency of PSC were investigated by a Keithley 2400 instrument under simulated AM 1.5G light (SAN-EI, XES-40S3) from +1.2 V to −0.1 V with a 50 ms scanning delay.

Label Visualization and Image Preprocessing: A converting process was used to visualize both the label and the predicted label. Using the label “Red” as an example, assuming that the RGB value of one pixel is [255,0,0] with a corresponding label value of 0 (0 representing “Red”), label 0 was replaced by [255,134,134] during the visualization process. By processing three-channel RGB data from the input image, it converted the pixel data into corresponding photo-pulses of three different wavebands, which are then fed into the sub-reservoir. The optical signal was converted into three-length features, which were then received by the readout layer. Its color was classified and identified using two fully connected layers. Details about the simulation method are provided in the Supporting Information (Supporting Method and Figure S19, Supporting Information).

Supporting Information

Supporting Information is available from the Wiley Online Library or from the author.

Acknowledgements

This study has been supported by the National Key Research and Development Program of China (No. 2023YFE0208600 and No. 2022YFB3803300), the National Natural Science Foundation of China (No. 62375288, No. U23A20138 and No. 52173192), the State Key Laboratory of Precision Manufacturing for Extreme Service Performance, Central South University (No. ZZYJKT2023-10), the Research Foundation of Education Bureau of Hunan Province (No. 23B0010), and Fundamental Research Funds for the Central Universities of Central South University (No. 1053320222260).

Conflict of Interest

The authors declare no conflict of interest.

Author Contributions

C.J., J.W., S.Y., and Y.D. contributed equally to this work. C.J., J.S., and J.Y. conceived the original concept and designed the experiments. S.Y., C.J., J.C., and Y.D. fabricated the devices and characterized its performance. W.J. simulated and calculated the data. W.L., Y.X., X.S., P.X., C.W., Z.Z., J.C.H., L.L., J.S., and J.Y. contributed to analysis and discussion on the data. C.J., S.Y., and W.J. wrote the manuscript with input from all the other authors. All authors discussed the results and commented on the manuscript.

Data Availability Statement

The data that support the findings of this study are available in the supplementary material of this article.

Keywords

dynamic color recognition, motion detection, neuromorphic visual sensor, photovoltage-driven oxide transistors

Received: July 18, 2024

Revised: October 14, 2024

Published online: October 28, 2024

- [1] M. Lee, G. J. Lee, H. J. Jang, E. Joh, H. Cho, M. S. Kim, H. M. Kim, K. M. Kang, J. H. Lee, M. Kim, H. Jang, J.-E. Yeo, F. Durand, N. Lu, D.-H. Kim, Y. M. Song, *Nat. Electron.* **2022**, *5*, 452.
- [2] S. Subbulakshmi Radhakrishnan, S. Chakrabarti, D. Sen, M. Das, T. F. Schranghamer, A. Sebastian, S. Das, *Adv. Mater.* **2022**, *34*, 2202535.
- [3] F. Zhou, Z. Zhou, J. Chen, T. H. Choy, J. Wang, N. Zhang, Z. Lin, S. Yu, J. Kang, H. P. Wong, Y. Chai, *Nat. Nanotechnol.* **2019**, *14*, 776.
- [4] L. Mennel, J. Symonowicz, S. Wachter, D. K. Polyushkin, A. J. Molina-Mendoza, T. Mueller, *Nature* **2020**, *579*, 62.
- [5] W. Alquraishi, J. Sun, W. Qiu, W. Liu, Y. Huang, C. Jin, Y. Gao, *Appl. Phys. A* **2020**, *126*, 431.
- [6] M. Kilpelainen, N. M. Putnam, K. Ratnam, A. Roorda, *J. Vis.* **2021**, *21*, 9.
- [7] C. McCollough, *Science* **1965**, *149*, 1115.
- [8] C. A. Párraga, T. Troscianko, D. J. Tolhurst, *Curr. Biol.* **2000**, *10*, 35.
- [9] S. Thorpe, D. Fize, C. Marlot, *Nature* **1996**, *381*, 520.
- [10] D. J. Heslenfeld, J. L. Kenemans, A. Kok, P. C. M. Molenaar, *Biol. Psychol.* **1997**, *45*, 183.
- [11] S. E. Ng, N. Yantara, N. A. Tu, E. Erdenebileg, P. W. F. Li, D. Sharma, Y. M. Lam, S. Mhaisalkar, A. Basu, A. Chattopadhyay, N. Mathews, *Adv. Mater.* **2024**, *36*, 2406568.
- [12] P. Bhatnagar, M. Patel, K. Lee, J. Kim, *InfoMat* **2023**, *5*, e12408.
- [13] J. Xue, Z. Zhu, X. Xu, Y. Gu, S. Wang, L. Xu, Y. Zou, J. Song, H. Zeng, Q. Chen, *Nano Lett.* **2018**, *18*, 7628.
- [14] X. Zhu, C. Gao, Y. Ren, X. Zhang, E. Li, C. Wang, F. Yang, J. Wu, W. Hu, H. Chen, *Adv. Mater.* **2023**, *35*, 2301468.
- [15] H. Tan, S. van Dijken, *Nat. Commun.* **2023**, *14*, 2169.
- [16] R. Siminoff, *Biol. Cybern.* **1991**, *64*, 505.
- [17] R. Sabesan, B. P. Schmidt, W. S. Tuten, A. Roorda, *Sci. Adv.* **2016**, *2*, e1600797.
- [18] C. M. Yang, T. C. Chen, D. Verma, L. J. Li, B. Liu, W. H. Chang, C. S. Lai, *Adv. Funct. Mater.* **2020**, *30*, 2001598.
- [19] Z. Shen, C. Zhang, Y. Meng, Z. Wang, *ACS Appl. Mater. Interfaces* **2022**, *14*, 32412.
- [20] F. Liao, Z. Zhou, B. J. Kim, J. Chen, J. Wang, T. Wan, Y. Zhou, A. T. Hoang, C. Wang, J. Kang, J.-H. Ahn, Y. Chai, *Nat. Electron.* **2022**, *5*, 84.
- [21] S. M. Kwon, J. Y. Kwak, S. Song, J. Kim, C. Jo, S. S. Cho, S. J. Nam, J. Kim, G. S. Park, Y. H. Kim, S. K. Park, *Adv. Mater.* **2021**, *33*, 2105017.
- [22] T. Ahmed, S. Kuriakose, S. Abbas, M. J. S. Spencer, M. A. Rahman, M. Tahir, Y. Lu, P. Sonar, V. Bansal, M. Bhaskaran, S. Sriram, S. Walia, *Adv. Funct. Mater.* **2019**, *29*, 1901991.
- [23] C.-Y. Wang, S.-J. Liang, S. Wang, P. Wang, Z. A. Li, Z. Wang, A. Gao, C. Pan, C. Liu, J. Liu, H. Yang, X. Liu, W. Song, C. Wang, B. Cheng, X. Wang, K. Chen, Z. Wang, K. Watanabe, T. Taniguchi, J. J. Yang, F. Miao, *Sci. Adv.* **2020**, *6*, eaba6173.
- [24] L. Pi, P. Wang, S.-J. Liang, P. Chen, X. Zhou, F. Miao, P. Luo, T. Zhai, *Nat. Electron.* **2022**, *5*, 248.
- [25] Z. Zhang, S. Wang, C. Liu, R. Xie, W. Hu, P. Zhou, *Nat. Nanotechnol.* **2021**, *17*, 27.
- [26] J. Song, G. Tang, J. Cao, H. Liu, Z. Zhao, S. Griggs, A. Yang, N. Wang, H. Cheng, C. K. Liu, I. McCulloch, F. Yan, *Adv. Mater.* **2023**, *35*, 2207763.

- [27] Y. Li, G. Chen, S. Zhao, C. Liu, N. Zhao, *Sci. Adv.* **2022**, 8, eabq0187.
- [28] C. T. Liu, S. Luryi, *Appl. Phys. Lett.* **1991**, 9, 393.
- [29] M. Albanna, K. W. Binder, S. V. Murphy, J. Kim, S. A. Qasem, W. Zhao, J. Tan, I. B. El-Amin, D. D. Dice, J. Marco, J. Green, T. Xu, A. Skardal, J. H. Holmes, J. D. Jackson, A. Atala, J. J. Yoo, *Sci. Rep.* **2019**, 9, 1856.
- [30] J. Zhu, Y. Yang, R. Jia, Z. Liang, W. Zhu, Z. U. Rehman, L. Bao, X. Zhang, Y. Cai, L. Song, R. Huang, *Adv. Mater.* **2018**, 30, 1800195.
- [31] L. Q. Zhu, C. J. Wan, L. Q. Guo, Y. Shi, Q. Wan, *Nat. Commun.* **2014**, 5, 3158.
- [32] C. Jin, W. Liu, Y. Xu, Y. Huang, Y. Nie, X. Shi, G. Zhang, P. He, J. Zhang, H. Cao, J. Sun, J. Yang, *Nano Lett.* **2022**, 22, 3372.
- [33] S. Hong, S. H. Choi, J. Park, H. Yoo, J. Y. Oh, E. Hwang, D. H. Yoon, S. Kim, *ACS Nano* **2020**, 14, 9796.
- [34] R. A. John, N. Yantara, S. E. Ng, M. I. B. Patdillah, M. R. Kulkarni, N. F. Jamaludin, J. Basu, Ankit, S. G. Mhaisalkar, A. Basu, N. Mathews, *Adv. Mater.* **2021**, 33, 2007851.
- [35] S. Qin, C. Lu, Z. Jia, Y. Wang, S. Li, W. Lai, P. Shi, R. Wang, C. Zhu, J. Du, J. Zhang, L. Meng, Y. Li, *Adv. Mater.* **2022**, 34, 2108829.
- [36] K. Xiao, Y.-H. Lin, M. Zhang, R. D. J. Oliver, X. Wang, Z. Liu, X. Luo, J. Li, D. Lai, H. Luo, R. Lin, J. Xu, Y. Hou, H. J. Snaith, H. Tan, *Science* **2022**, 376, 762.
- [37] Q. Dong, Y. Fang, Y. Shao, P. Mulligan, J. Qiu, L. Cao, J. Huang, *Science* **2015**, 347, 967.
- [38] R. Sharma, A. Sharma, S. Agarwal, M. S. Dhaka, *Sol. Energy* **2022**, 244, 516.
- [39] J. Lim, M. Kober-Czerny, Y.-H. Lin, J. M. Ball, N. Sakai, E. A. Duijnste, M. J. Hong, J. G. Labram, B. Wenger, H. J. Snaith, *Nat. Commun.* **2022**, 13, 4201.
- [40] T. Yang, L. Gao, J. Lu, C. Ma, Y. Du, P. Wang, Z. Ding, S. Wang, P. Xu, D. Liu, H. Li, X. Chang, J. Fang, W. Tian, Y. Yang, S. F. Liu, K. Zhao, *Nat. Commun.* **2023**, 14, 839.
- [41] H. Zhang, X. Ji, H. Yao, Q. Fan, B. Yu, J. Li, *Sol. Energy* **2022**, 233, 421.
- [42] U. R. Karmarkar, Y. Dan, *Neuron* **2006**, 52, 577.
- [43] V. K. Taylor, D. S. Schwarzkopf, A. H. Dahlmann-Noor, *Curr. Opin. Neurol.* **2017**, 30, 74.
- [44] S. Wang, C. Y. Wang, P. Wang, C. Wang, Z. A. Li, C. Pan, Y. Dai, A. Gao, C. Liu, J. Liu, H. Yang, X. Liu, B. Cheng, K. Chen, Z. Wang, K. Watanabe, T. Taniguchi, S. J. Liang, F. Miao, *Natl. Sci. Rev.* **2021**, 8, nwaa172.
- [45] R. H. Masland, *Nat. Neurosci.* **2001**, 4, 877.
- [46] D. A. Atchison, *Optics of the Human Eye*, CRC Press, Boca Raton, Florida **2023**.
- [47] A. Daus, C. Vogt, N. Münzenrieder, L. Petti, S. Knobelspies, G. Cantarella, M. Luisier, G. A. Salvatore, G. Tröster, *J. Appl. Phys.* **2016**, 120, 244501.
- [48] A. Daus, C. Vogt, N. Munzenrieder, L. Petti, S. Knobelspies, G. Cantarella, M. Luisier, G. A. Salvatore, G. Troster, *IEEE Trans. Electron Devices* **2017**, 64, 2789.
- [49] K. Kumari, S. Majumder, A. D. Thakur, S. J. Ray, *Mater. Lett.* **2021**, 303, 130451.
- [50] L. Li, K.-C. Chang, X. Lin, Y.-C. Lai, R. Zhang, T.-P. Kuo, *Nanoscale* **2020**, 12, 15721.
- [51] B. Mu, L. Guo, J. Liao, P. Xie, G. Ding, Z. Lv, Y. Zhou, S. T. Han, Y. Yan, *Small* **2021**, 17, e2103837.
- [52] H. Wang, Q. Zhao, Z. Ni, Q. Li, H. Liu, Y. Yang, L. Wang, Y. Ran, Y. Guo, W. Hu, Y. Liu, *Adv. Mater.* **2018**, 30, 1803961.
- [53] C. Han, X. Han, J. Han, M. He, S. Peng, C. Zhang, X. Liu, J. Gou, J. Wang, *Adv. Funct. Mater.* **2022**, 32, 2113053.
- [54] Y. Zhong, J. Tang, X. Li, X. Liang, Z. Liu, Y. Li, Y. Xi, P. Yao, Z. Hao, B. Gao, H. Qian, H. Wu, *Nat. Electron.* **2022**, 5, 672.
- [55] K. Liu, T. Zhang, B. Dang, L. Bao, L. Xu, C. Cheng, Z. Yang, R. Huang, Y. Yang, *Nat. Electron.* **2022**, 5, 761.
- [56] Y. Zhou, J. Fu, Z. Chen, F. Zhuge, Y. Wang, J. Yan, S. Ma, L. Xu, H. Yuan, M. Chan, X. Miao, Y. He, Y. Chai, *Nat. Electron.* **2023**, 6, 870.
- [57] K. Liu, B. Dang, T. Zhang, Z. Yang, L. Bao, L. Xu, C. Cheng, R. Huang, Y. Yang, *Adv. Mater.* **2022**, 34, 2108826.